Effect of a magnetic field gradient and gravitational acceleration on a time-domain grating-echo interferometer

M. Weel, I. Chan, S. Beattie, and A. Kumarakrishnan
Department of Physics and Astronomy, York University, Toronto, Ontario, Canada M3J 1P3

D. Gosset
Department of Physics and Astronomy, University of British Columbia, Vancouver, British Columbia, Canada V6T 1Z1

I. Yavin
Department of Physics, Harvard University, Cambridge, Massachusetts 02138, USA

(Received 30 August 2005; revised manuscript received 12 December 2005; published 28 June 2006)

We have observed the effects of magnetic field gradients and gravitational acceleration on grating echoes in a time-domain single state atom interferometer that uses laser cooled Rb atoms. These observations are compared to theoretical predictions based on a simplified model. The oscillatory dependence of the echo amplitude due to the magnetic field gradient is in agreement with the predicted quadratic scaling as a function of the time between excitation pulses. We also observe a linear dependence of this oscillation frequency as a function of the magnetic field gradient which is predicted by theory. In the presence of gravity, the calculations predict a quadratic dependence for the echo phase on the time between excitation pulses as well as a change in the shape of the echo envelope. We have observed both of these effects in the experiment, and we find that the change in shape is qualitatively consistent with our prediction. It is necessary to understand these effects in order to carry out high precision studies of the atomic fine-structure constant and gravitational acceleration using this interferometric technique. We also present an improved measurement of gravitational acceleration using this technique that is precise to ~15 ppm by exploiting the quadratic phase dependence.

DOI: 10.1103/PhysRevA.73.063624 PACS number(s): 03.75.Dg, 32.80.Pj, 42.50.Md, 42.50.Vk

I. INTRODUCTION

Atom interferometers (AIs) that use cold samples of neutral atoms have been used for precision measurements of the atomic fine-structure constant α [1–7] and for inertial sensing applications such as accurate determination of gravitational acceleration [8,9], rotation [10], and gravity gradients [11].

AIs are sensitive to the atomic recoil frequency $\omega_q = \frac{\hbar q^2}{2m_{atom}}$, where q is proportional to the momentum transferred to an atom by the laser fields. This quantity is related to the atomic fine-structure constant α. It has been recognized that AIs offer the potential for making one of the most precise measurements of α [12] and that the measurement accuracy is expected to surpass the most precise determination of α, which is based on a measurement of the electron g factor that is precise to 3.8 ppb [13].

The best measurements of α have been carried out using Raman transitions between hyperfine ground states of cesium atoms launched in an atomic fountain [1,4]. Although a statistical precision of a few parts per billion has been reached, systematic effects that are much larger remain to be reconciled [4]. The best interferometric measurements of gravitational acceleration g [9] and gravity gradients [11] have also been carried out using Raman transitions between hyperfine ground states.

Another promising interferometric approach for determining α has involved measurements of ω_q using single state interferometers, as first demonstrated in Ref. [2]. Since then, three different single state atom interferometric techniques have been demonstrated. These include experiments with dilute samples of trapped atoms [5–7] or much denser atomic clouds cooled to the transition temperature for Bose Einstein Condensation (BEC) [3,14]. In these experiments, cold atoms are manipulated in the same internal ground state using off resonant standing-wave pulses. This feature makes the experiment inherently less sensitive to systematic errors due to ac Stark shifts and magnetic fields and may offer the advantage of reduced experimental complexity in certain respects. As in experiments using Raman transitions, the precision associated with the single state techniques relies on the transit time of cold atoms through the region of interaction. Therefore if single state experiments are carried out in atomic fountains, it can be expected that they will achieve the same sensitivity as the experiments using Raman transitions.

Among the single state measurements, Refs. [2,5] are proof of principle studies using time-domain and frequency-domain techniques, respectively. The work in Ref. [3] has used a time-domain technique similar to Ref. [2] to achieve a precision of ~7 ppm. However, the precision was affected by systematic effects at the level of 10^{-4}, an effect that was attributed to inter atomic interactions in the BEC. The work in Ref. [6] has achieved a precision of 0.4 ppm but their results disagree at the level of 1.5 standard deviations with respect to the accepted value of α. The measurement in Ref. [7] is an extension of the work in Ref. [2] and is currently precise to 2.5 ppm. This result is also in excellent agreement (within 1 σ) with the value of ω_q obtained from measurements of the Rb transition wavelength at JILA [15] and atomic mass at MIT [16]. The most significant aspect of the work in Ref. [7] is that it has been possible to demonstrate

immunity of the technique to a variety of systematic effects such as ac Stark shifts, excitation pulse widths, magnetic fields, magnetic field gradients, atomic density, population distribution in the magnetic sublevels of the ground state, and spontaneous emission.

The main limitation on the time scale of the experiment in Ref. [7] is the presence of residual magnetic field gradients that limit the decay time of the signal. In fact, it can be expected that magnetic gradients affect all single state interferometers as shown in studies related to a scheme adapted for a single state chip based interferometer [17]. Thus it is important to understand the effect of the gradient on the interferometer and possible systematic effects on the recoil frequency. This would make it possible to design suitable shielding for fountain experiments.

The best atom interferometric measurements of gravity [9] and gravity gradients [11] have also involved Raman transitions in atoms launched in a cold atomic fountain. There has been an intense level of interest in such experiments for varied applications such as atom-based tests of the equivalence principle [18], which is based on differential gravity measurements in two Rb isotopes using an atomic fountain and the development of gravity gradiometers [11,19] for remote sensing using aircraft and satellites. Single state AIs have also demonstrated sensitivity to the acceleration due to gravity [2,20] and can offer the potential of exhibiting reduced sensitivity to a number of systematic effects. It can be expected that these experiments would result in the same precision as the Raman interferometers if the time scale is extended in a fountain and the inertial reference frame is actively stabilized as in Ref. [9]. However, the signal shape in the time-domain interferometer used in Refs. [7,20] is inherently sensitive to gravity. This effect has to be characterized and understood for carrying out high precision studies in a fountain.

In this paper we present calculations of the effects of magnetic gradients and gravity on the signal from our time-domain single state atom interferometer. We also compare the predictions to experimental results. The calculations confirm the oscillatory dependence of the signal on T in the presence of a magnetic field gradient as well as the dependence on the strength of the gradient. We have also confirmed that the signal shape for a fixed T is modified by gravity in a manner that is qualitatively consistent with predictions. The quadratic dependence of the signal phase on time between the pulses is used to obtain an improved measurement of gravity in comparison to Ref. [2]. The results also indicate that isolating the inertial reference frame from vibrations will allow a quantitative comparison with the signal shape that should improve the precision associated with the measurement of gravity. The rest of the paper is organized as follows. In the remainder of this section we outline the nature of our time-domain experiments. Section II gives a detailed theoretical description of the magnetic field gradient effect. Section III describes the experimental setup, and Sec. IV compares the results of the experiment with the theoretical predictions.

Outline of the experiment

The time-domain experiments in Refs. [2,7,20] rely on matter wave interference of laser-cooled rubidium atoms manipulated in a single atomic hyperfine ground state using pulsed standing-wave laser fields. The atoms are diffracted into a superposition of momentum states separated by multiples of $2\hbar k$ using an off resonant standing-wave pulse applied at $t=0$. The standing-wave interaction produces a spatially periodic density (grating) in the sample. This grating has a period of $\frac{\lambda}{2}$, where λ is the wavelength of light. Although the grating decays due to the velocity distribution of the sample, it can be rephased by a second off resonant standing-wave pulse (applied at $t=T$) in a manner reminiscent of a photon echo. In this case, the rephased density grating (echo) is produced in the vicinity of $t=2T$. The echo is detected using a heterodyne technique by coherently back scattering a traveling-wave readout pulse from the sample. The signal envelope exhibits a characteristic shape with a zero crossing at $t=2T$. The rephasing is a consequence of matter wave interference between different center-of-mass momentum states. Thus the AI relies on the discrete nature of atomic recoil (due to absorption and stimulated emission of photons between the traveling-wave components of the standing wave). In this case, the periodic dependence of the backscattered signal on pulse separation T is given by [2]

$$S \propto e^{-q^2u^2\Delta t^2/2} J_1[2\phi_1 \sin(-\omega_q \Delta t)] J_2[2\phi_2 \sin(-\omega_q T)]. \quad (1)$$

Here ϕ_1 and ϕ_2 are the pulse areas of the standing-wave pulses, $\Delta t=2T-t$ is the time measured with respect to the echo point, and u is the most probable speed of atoms in the sample along the direction of excitation. The first two terms in Eq. (1) define the signal shape (envelope) for a fixed T. The last term contains the periodic dependence of the signal on ω_q. It can be seen that the periodicity of the signal has a physical basis since a diffracted wave packet with a recoil velocity $v_r=\frac{\hbar q}{m_{atom}}$ can move through one grating wavelength $\frac{\lambda}{2}$ in time $\frac{\pi}{\omega_q}$ and interfere with an undiffracted wave packet. Here $q=2k$ for a standing-wave excitation. In Ref. [2], a preliminary measurement of ω_q was demonstrated by measuring the amplitude of the backscattered signal versus T and measuring the time between well-displaced zeroes. In Ref. [7], a more precise measurement of ω_q was obtained by carrying out the measurement over a longer time scale and by fitting to a modified expression for the signal shape to account for spontaneous emission and spatial profile of the excitation beams. One advantage of this method is that the phase of the scattered signal is not essential for the recoil measurement. Hence it is possible to carry out this experiment without special efforts to isolate the experiment from vibrations.

The echo technique finds widespread use because it a general method of canceling the effect of a velocity distribution in a sample. Our experiments are carried out in a sample of atoms with a temperature of ~ 100 μK. No velocity selection or additional cooling is necessary. The time at which the echo signal occurs corresponds to the time at which the accumulated Doppler phases of the atomic wave packets cancel.

In contrast to the recoil frequency measurements, measurements of gravity rely on the phase of the backscattered echo signal. The phase difference between momentum states

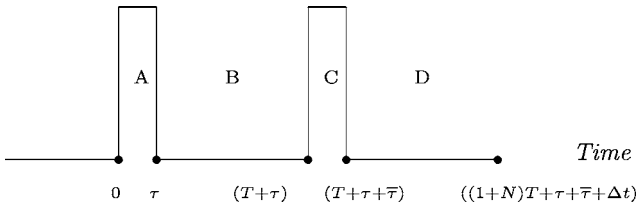

FIG. 1. Experiment timeline.

that interfere at the echo point scales as gT^2. This causes the phase of the backscattered signal to increment by 2π when the grating is displaced by one grating period $\left(\frac{\lambda}{2}\right)$ due to gravity. The phase of the signal is measured with reference to an optical local oscillator (LO). In this experiment, a mirror that serves as the inertial frame of reference has to be isolated from the effect of vibrations.

The decay of the echo amplitude should be determined primarily by the time of flight of atoms leaving the region of interaction. However, we find that the amplitude is an oscillatory function of a magnetic field gradient. In our experiments, a residual magnetic field gradient is present at the center of the vacuum chamber even after the turn off of the magnetic gradient coils used for trapping atoms. This effect is attributed to the magnetization of the chamber walls caused by the pulsed field gradient from the trapping coils. We have been able to achieve long time scales in the AI experiment [7] only by canceling this gradient with external coils and eliminating decoherence due to scattered light and collisions.

Although our results have shown that the recoil frequency ω_q is independent of magnetic field gradients up to 0.1 G/cm [7], the oscillatory dependence of the amplitude scales as T^2 and this makes it essential to understand and eliminate the effect. Similarly, understanding the effect of gravity could allow a more accurate determination of the phase by fitting to the echo signal envelope.

II. THEORETICAL MODEL

Signal calculation

Here we present a calculation of the atom interferometry signal when a magnetic field $\vec{B}=M\vec{x}$ is present throughout the experiment, where $M=\frac{dB}{dx}$ is the magnetic field gradient. To simplify the mathematics, we consider a strictly one-dimensional problem in which both the magnetic field and the atomic motion are considered only along the vertical (x-axis). In addition, we ignore the effect of gravity. This work extends the calculation of the echo signal in Ref. [2]. The experimental pulse sequence is shown in Fig. 1; the pulse widths are designated by τ and $\bar{\tau}$ and their separation is represented by T. The echo is observed in the vicinity of $2T$. We assume the pulse widths to be in the Raman-Nath regime since the typical distance traveled by the atom during the excitation pulse is small compared to the wavelength of the standing wave.

We note that the echo signal should be calculated for each magnetic sublevel of the $F=3$ ground state. A uniform population distribution in the sublevels can be expected in low density Magneto Optical Traps (MOTs) in the absence of radiation trapping. However, in the presence of radiation trapping polarization gradient cooling results in preferential population of the high $|m|$ sublevels as described in experiments with Cs MOTs [21]. We have observed the same effects in Rb MOTs [22]. Details of the characterization of level populations and release of atoms from the trap are described in Sec. III.

The experiment uses circularly polarized standing-wave pulses and a circularly polarized readout pulse to detect the backscattered signal. If the standing-wave excitation is blue detuned and far off resonance the signal from each of the sublevels of the $F=3$ ground state can be described following the treatment in Ref. [23]. Assuming that the population is only in the $m=\pm 3$ sublevels, the backscattered signal is the sum of independent contributions, which are given by

$$S_{m=3} \propto (C_{3,4'})^2 e^{-q^2u^2\Delta t^2/2} J_1[2\phi_{1,3}\sin(-\omega_q\Delta t)] \times J_2[2\phi_{2,3}\sin(-\omega_q T)]$$

and

$$S_{m=-3} \propto (C_{-3,-2'})^2 e^{-q^2u^2\Delta t^2/2} J_1[2\phi_{1,-3}\sin(-\omega_q\Delta t)] \times J_2[2\phi_{2,-3}\sin(-\omega_q T)],$$

respectively.

Here $\phi_{1,3}$ and $\phi_{1,-3}$ are the pulse areas for excitation of each sublevel. $\phi_{1,3}=-C_{3,4'}\frac{\Omega^2}{8\Delta}$ and $\phi_{1,-3}=-C_{-3,-2'}\frac{\Omega^2}{8\Delta}$ are defined in terms of the Rabi frequency of the excitation pulse Ω, Δ is the detuning of the excitation pulses with respect to the $F=3$ to $F=4'$ transition, and $C_{3,4'}=1$ and $C_{-3,-2'}=\sqrt{1/28}$ are the Clebch-Gordon coefficients. We have assumed that couplings to the $F=3$ and $F=2$ excited states are negligible. It is clear that the individual terms are weighted by relevant transition properties. As a result the contribution of the signal from the $m=-3$ sublevel is generally much smaller than the contribution from the $m=3$ sublevel. Therefore the system can be modeled with all atoms in the $m=3$ state.

1. Hamiltonian

The effective Hamiltonian for the ground state of a single two-level atom in an off resonant standing-wave laser field with each traveling-wave component having wavelength $\lambda=\frac{2\pi}{k}$ is [7]

$$H=\frac{\hat{p}^2}{2m_{Rb}}+\frac{\hbar\Omega^2}{8(\Delta+i\Gamma)}\cos 2kx, \tag{2}$$

where Δ is the detuning of the laser frequency from the atomic resonance, Γ is the excited-state decay rate, and Ω is the Rabi frequency. We will take $q=2k$ in what follows. In this calculation we neglect Γ as in Ref. [2]. When a magnetic field is introduced, an additional term due to the interaction of the magnetic dipole moment of the atom with the field is introduced to the Hamiltonian:

$$H_{mag}=-\vec{\mu}\cdot\vec{B}. \tag{3}$$

Here μ is the atom's magnetic dipole moment which arises due to electron spin, electron orbital, and nuclear-spin angular momentum. In the case of a ^{85}Rb atom in the $F=3$ ground state, we have total orbital angular momentum $L=0$, electron spin angular momentum $S=\frac{1}{2}$, and nuclear-spin angular momentum $I=\frac{5}{2}$. Since the nuclear magneton is smaller than the bohr magneton by a factor of $\sim\frac{m_e}{m_p}$, we disregard the interaction of the nucleus with the external magnetic field. Since $L=0$, we take $\mu=-\frac{g_s\mu_B}{\hbar}\vec{S}$ and write

$$H_{mag}=-\frac{g_s\mu_B}{\hbar}\vec{S}\cdot\vec{B}. \tag{4}$$

We now substitute $\vec{B}=M\vec{x}$, $\mu_B=\frac{e\hbar}{2m_e}$, and $g_s\simeq 2$ to obtain

$$H_{mag}=\frac{e}{m_e}MS_x x. \tag{5}$$

2. Region A: $0\le t\le\tau$

We begin by using the Raman-Nath approximation to determine the time evolution of the atomic wave functions during the first excitation pulse. This allows us to disregard the kinetic energy term in the Hamiltonian. We take an atom's initial wave function $\Psi(0)$ to be the momentum eigenstate with wave number k_0 and spin state

$$\begin{pmatrix} a \\ b \end{pmatrix}$$

in a basis of S_x eigenstates. We can then calculate the atomic wave function after the first pulse:

$$\Psi(\tau)=e^{-(i/\hbar)\int_0^\tau V(x)dt}\Psi(0), \tag{6}$$

$$\Psi(\tau)=e^{-(i/\hbar)\int_0^\tau(\Omega^2\hbar/8\Delta)\cos\, qx+(eMxS_x/m_e)dt}e^{ik_0x}\begin{pmatrix} a \\ b \end{pmatrix} \tag{7}$$

$$=e^{i(\phi_1\cos\, qx+k_0x)}\begin{pmatrix} e^{-ieMx\tau/2m_e} & 0 \\ 0 & e^{ieMx\tau/2m_e} \end{pmatrix}\begin{pmatrix} a \\ b \end{pmatrix}. \tag{8}$$

In the above expression we have taken the pulse area $\phi_1=-\frac{\Omega^2\tau}{8\Delta}$. We now make use of the Jacobi-Anger expansion [24]:

$$\Psi(\tau)=\sum_{n=-\infty}^{\infty}(i)^nJ_n(\phi_1)e^{i(nq+k_0)x}\begin{pmatrix} ae^{\frac{-ieMx\tau}{2m_e}} \\ be^{\frac{ieMx\tau}{2m_e}} \end{pmatrix}. \tag{9}$$

3. Region B: $\tau\le t\le\tau+T$

In this region, the Hamiltonian is $H=\frac{\hat{p}^2}{2m_{Rb}}+\frac{eMS_xx}{m_e}$. We now use the associated time evolution operator $e^{(-i/\hbar)\int_0^T H(t')dt'}$ on the result from Eq. (9):

$$\Psi(T+\tau)=\sum_{n=-\infty}^{\infty}\left[(i)^nJ_n(\phi_1)e^{-i\hat{p}^2T/2m_{Rb}\hbar-iemTS_xx/\hbar m_e}\times e^{i(nq+k_0)x}\begin{pmatrix} ae^{-ieMx\tau/2m_e} \\ be^{ieMx\tau/2m_e} \end{pmatrix}\right]. \tag{10}$$

We now make use of the operator identity known as the Zassenhaus formula [25]. From that formula it can be shown directly that for two operators A and B which satisfy $[A,[A,B]]\in\mathbb{C}$ and $[B,[A,B]]=0$, we have the following relation:

$$e^{A+B}=e^Ae^Be^{-[A,B]/2}e^{[A,[A,B]]/6}. \tag{11}$$

We take $A=\frac{-ieMTS_xx}{\hbar m_e}$ and $B=\frac{-iT\hat{p}^2}{2\hbar m_{Rb}}$. The commutators are as follows:

$$[A,B]=\frac{eMT^2S_x}{2\hbar^2m_{Rb}m_e}[\hat{p}^2,x] \tag{12}$$

$$=\frac{-ieMT^2S_x}{\hbar m_{Rb}m_e}\hat{p}, \tag{13}$$

$$[B,[A,B]]=0, \tag{14}$$

$$[A,[A,B]]=\frac{-e^2M^2T^3\hbar^2}{4\hbar^2m_{Rb}m_e^2}[x,p] \tag{15}$$

$$=DT^3. \tag{16}$$

Here $D=ib$, where b is a real number. We may use Eq. (11) to write

$$e^{-ieMTS_xx/\hbar m_e-+iT\hat{p}^2/2\hbar m_{Rb}}=e^{-ieMTS_xx/\hbar m_e}e^{-iT\hat{p}^2/2\hbar m_{Rb}}e^{(ieMT^2S_x/2\hbar m_{Rb}m_e)\hat{p}}e^{DT^3/6}. \tag{17}$$

We can now write an expression for the atomic wave function after time $\tau+T$ using the above and our result from Eq. (10):

$$\Psi(\tau+T)=\sum_{n=-\infty}^{\infty}\left[(i)^nJ_n(\phi_1)e^{-ieMTS_xx/\hbar m_e}\times e^{-iT\hat{p}^2/2\hbar m_{Rb}}e(ieMT^2S_x/2\,\hbar\, m_{Rb}m_e)\hat{p}\times e^{DT^3/6}e^{i(nq+k_0)x}\begin{pmatrix} ae^{-ieMx\tau/2m_e} \\ be^{ieMx\tau/2m_e} \end{pmatrix}\right].$$

We now use the formula for spin rotations (in a basis of S_x eigenstates):

$$e^{iSx\theta}=\begin{pmatrix} e^{i\hbar\theta/2} & 0 \\ 0 & e^{-i\hbar\theta/2} \end{pmatrix}, \tag{18}$$

$$\Psi(\tau+T) = e^{DT^3/6}\sum_{n=-\infty}^{\infty}\left[(i)^n J_n(\phi_1)e^{-ieMTS_x x/\hbar m_e}e^{-iT\hat{p}^2/2\hbar m_{Rb}}\begin{pmatrix} e^{(ieMT^2/4m_{Rb}m_e)\hat{p}} & 0 \\ 0 & e^{(-ieMT^2/4mm_e)\hat{p}}\end{pmatrix}\begin{pmatrix} ae^{-ieMx\tau/2m_e+i(nq+k_0)x} \\ be^{ieMx\tau/2m_e+i(nq+k_0)x}\end{pmatrix}\right]$$

$$= e^{DT^3/6}\sum_{n=-\infty}^{\infty}\left[(i)^n J_n(\phi_1)e^{-ieMTS_x x/\hbar m_e}e^{-iT\hat{p}^2/2\hbar m}\begin{pmatrix} ae^{-ieMx\tau/2m_e+i(nq+k_0)x+ieMT^2/4m_{Rb}m_e\hbar(nq+k_0-eM\tau/2m_e)} \\ be^{ieMx\tau/2m_e+i(nq+k_0)x-ieMT^2/4m_{Rb}m_e\hbar(nq+k_0+eM\tau/2m_e)}\end{pmatrix}\right]$$

$$= e^{DT^3/6}\sum_{n=-\infty}^{\infty}\left[(i)^n J_n(\phi_1)\begin{pmatrix} e^{-ieMTx/2m_e} & 0 \\ 0 & e^{ieMTx/2m_e}\end{pmatrix}\right.$$

$$\left.\times\begin{pmatrix} ae^{-ieMx\tau/2m_e+i(nq+k_0)x+(ieMT^2/4m_{Rb}m_e)\hbar(nq+k_0-eM\tau/2m_e)} & e^{-(iT\hbar/2m_{Rb})[-eM\tau/2m_e+(nq+k_0)]^2} \\ be^{ieMx\tau/2m_e+i(nq+k_0)x-(ieMT^2/4m_{Rb}m_e)\hbar(nq+k_0+eM\tau/2m_e)} & e^{-(iT\hbar/2m_{Rb})[eM\tau/2m_e+(nq+k_0)]^2}\end{pmatrix}\right]$$

$$= e^{DT^3/6}\sum_{n=-\infty}^{\infty}\left[(i)^n J_n(\phi_1)\begin{pmatrix} ae^{-ieMx(T+\tau)/2m_e+i(nq+k_0)x+(ieMT^2/4m_{Rb}m_e)\hbar(nq+k_0-eM\tau/2m_e)} & e^{-(iT\hbar/2m_{Rb})[-eM\tau/2m_e+(nq+k_0)]^2} \\ be^{ieMx(T+\tau)/2m_e+i(nq+k_0)x-(ieMT^2/4m_{Rb}m_e)\hbar(nq+k_0+eM\tau/2m_e)} & e^{-(iT\hbar/2m_{Rb})[eM\tau/2m_e+(nq+k_0)]^2}\end{pmatrix}\right]. \tag{19}$$

4. Region C: $T+\tau \le t \le T+\tau+\bar{\tau}$

In this region the atom is again subjected to a standing-wave radiation pulse. We again use the Raman-Nath approximation as well as the Jacobi-Anger expansion:

$$\Psi(\tau+\bar{\tau}+T) = e^{DT^3/6}\sum_{n=-\infty}^{\infty}\sum_{n'=-\infty}^{\infty}\left[(i)^{n+n'}J_n(\phi_1)J_{n'}(\phi_2)\right.$$

$$\left.\times\begin{pmatrix} ae^{-ieMx(T+\tau+\tau)/2m_e+i[(n+n')q+k_0]x+ieMT^2/4m_{Rb}m_e\hbar(nq+k_0-eM\tau/2m_e)-(iT\hbar/2m_{Rb})[-eM\tau/2m_e+(nq+k_0)]^2} \\ be^{ieMx(T+\tau+\tau)/2m_e+i[(n+n')q+k_0]x-ieMT^2/4m_{Rb}m_e\hbar(nq+k_0+eM\tau/2m_e)-(iT\hbar/2m_{Rb})[eM\tau/2m_e+(nq+k_0)]^2}\end{pmatrix}\right], \tag{20}$$

where $\phi_2 = -\frac{\Omega^2\bar{\tau}}{8\Delta}$.

5. Region D: $T+\tau+\bar{\tau} \le t \le (1+N)T+\tau+\bar{\tau}+\Delta t$

Following the method of region *B*, we may express the wave function at a time $t_0 = NT+\Delta t$ after the second radiation pulse:

$$\Psi(T+\tau+\bar{\tau}+t_0)$$

$$= e^{-ieMt_0S_x x/\hbar m_e}e^{-it_0\hat{p}^2/2\hbar m_{Rb}}e^{(ieMt_0^2S_x/2\hbar m_{Rb}m_e)\hat{p}}e^{Dt_0^3/6}\Psi(T+\tau+\bar{\tau})$$

$$= e^{D(T^3+t_0^3)/6}\sum_{n=-\infty}^{\infty}\sum_{n'=-\infty}^{\infty}\left[(i)^{n+n'}J_n(\phi_1)J_{n'}(\phi_2)e^{i[(n+n')q+k_0]x}e^{(-ieMt_0^2/4m_{Rb}m_e)\hbar[eM(T+\tau+\tau)/2m_e]}\right.$$

$$\left.\times\begin{pmatrix} ae^{-ieMx(T+\tau+\tau+t_0)/2m_e+(ieMT^2/4m_{Rb}m_e)\hbar(nq+k_0-eM\tau/2m_e)-(iT\hbar/2m_{Rb})[-eM\tau/2m_e+(nq+k_0)]^2+(ieMt_0^2/4m_{Rb}m_e)\hbar[(n+n')q+k_0]-(it_0\hbar/2m_{Rb})[(n+n')q+k_0]-eM(T+\tau+\tau)/2m_e^2} \\ be^{ieMx(T+\tau+\tau+t_0)/2m_e-(ieMT^2/4m_{Rb}m_e)\hbar(nq+k_0+eM\tau/2m_e)-(iT\hbar/2m_{Rb})[eM\tau/2m_e+(nq+k_0)]^2-(ieMt_0^2/4m_{Rb}m_e)\hbar[(n+n')q+k_0]-(it_0\hbar/2m_{Rb})[[(n+n')q+k_0]+eM(T+\tau+\tau)/2m_e]^2}\end{pmatrix}\right]. \tag{21}$$

6. Interferometry signal

The interferometry signal is obtained by backscattering a traveling wave of wavelength $\lambda = \frac{2\pi}{k}$ from the sample. In order to determine the form of this signal, we first calculate the atomic probability density $\Psi^*\Psi$, and then determine the Fourier components with spatial frequency $q=2k$, which are the only components detected by this method,

$$\Psi^*\Psi = \sum_{\substack{-\infty<n<\infty \\ -\infty<n'<\infty}} \sum_{\substack{-\infty<l<\infty \\ -\infty<l'<\infty}} (i)^{n+n'-(l+l')} J_n(\phi_1) J_{n'}(\phi_2) J_l(\phi_1) J_{l'}(\phi_2) e^{i[(n+n')-(l+l')]qx}$$
$$\times [(|a|^2 e^{(ieMT^2\hbar/4m_{Rb}m_e)(n-l)q} e^{-(iT\hbar/2m_{Rb})[(n^2-l^2)q^2+2qk_0(n-l)+2(n-l)q(-eM\tau/2m_e)]} e^{(ieMt_0^2/4m_{Rb}m_e)\hbar[(n+n')-(l+l')]q})$$
$$\times e^{-(it_0\hbar/2m_{Rb})\{[(n+n')^2-(l+l')^2]q^2+2qk_0[(n+n')-(l+l')]+2[(n+n')-(l+l')]q[-eM(T+\tau+\bar{\tau})/2m_e]\}}$$
$$+ (|b|^2 e^{(-ieMT^2\hbar/4m_{Rb}m_e)(n-l)q} e^{-(iT\hbar/2m_{Rb})[(n^2-l^2)q^2+2qk_0(n-l)+2(n-l)q(eM\tau/2m_e)]} e^{(-ieMt_0^2/4m_{Rb}m_e)\hbar[(n+n')-(l+l')]q})$$
$$\times e^{-(it_0\hbar/2m)\{[(n+n')^2-(l+l')^2]q^2+2qk_0[(n+n')-(l+l')]+2[(n+n')-(l+l')]q[eM(T+\tau+\bar{\tau})/2m_e]\}}]. \quad (22)$$

We now introduce some definitions, as well as restrictions on the summation variables. The restrictions ensure that only momentum states whose classical trajectories overlap at time $t=NT$ contribute to the signal [23,26–28]. For our experiment $N=1$, which corresponds to the echo at $t\sim 2T$:

$$v_0 = \frac{\hbar k_0}{m_{Rb}}, \quad \Delta t = t_0 - NT, \quad (23)$$

$$\omega_q = \frac{\hbar q^2}{2m_{Rb}}, \quad N = \frac{l-n}{s}, \quad (24)$$

$$\omega_0 = \frac{\hbar k_0^2}{2m_{Rb}}, \quad s = (n+n') - (l+l'). \quad (25)$$

Substituting into Eq. (22):

$$\Psi^*\Psi = \sum_{-\infty<s<\infty} \sum_{\substack{-\infty<n<\infty \\ -\infty<n'<\infty}} (i)^s J_n(\phi_1) J_{n'}(\phi_2) J_{n+sN}(\phi_1) J_{n'-s(N+1)}(\phi_2) e^{isqx} [(|a|^2 e^{(ieMT^2\hbar/4m_{Rb}m_e)(-sN)q} e^{iT\omega_q(sN)(2n+sN)} e^{iTqv_0sN}$$
$$\times e^{-iseM\hbar NT\tau q/2m_{Rb}m_e} e^{(ieMt_0^2/4m_{Rb}m_e)\hbar sq} e^{-it_0\omega_q s[2(n+n')-s]} e^{-it_0 sqv_0} e^{(ieM\hbar sqt_0/2m_{Rb}m_e)(T+\tau+\bar{\tau})}) + (|b|^2 e^{(-ieMT^2\hbar/4m_{Rb}m_e)(-sN)q}$$
$$\times e^{iT\omega_q(sN)(2n+sN)} e^{iTqv_0sN} e^{iseM\hbar NT\tau q/2m_{Rb}m_e} e^{(-ieMt_0^2/4m_{Rb}m_e)\hbar sq} e^{-it_0\omega_q s[2(n+n')-s]} e^{-it_0 sqv_0} e^{(-ieM\hbar sqt_0/2m_{Rb}m_e)(T+\tau+\bar{\tau})})]$$
$$= \sum_{-\infty<s<\infty} \sum_{\substack{-\infty<n<\infty \\ -\infty<n'<\infty}} (i)^s J_n(\phi_1) J_{n'}(\phi_2) J_{n+sN}(\phi_1) J_{n'-s(N+1)}(\phi_2) e^{isqx} e^{iT\omega_q(sN)(2n+sN)} e^{-iqv_o s\Delta t} e^{-it_0\omega_q s[2(n+n')-s]} (|a|^2 e^{\gamma} + |b|^2 e^{-\gamma}), \quad (26)$$

where $\gamma = \frac{ieMT^2\hbar}{4m_{Rb}m_e}(-sN)q - \frac{iseM\hbar NT\tau q}{2m_{Rb}m_e} + \frac{ieMt_0^2}{4m_{Rb}m_e}\hbar sq + \frac{ieM\hbar sqt_0}{2m_{Rb}m_e}(T+\tau+\bar{\tau})$. We can obtain a final expression for the probability density which has only one summation variable if we make use of the following Bessel function identity:

$$(i)^v J_v\left[2u\sin\left(\frac{a}{2}\right)\right] = \sum_{-\infty<l<\infty} e^{iva/2} J_{l+v}(u) J_l(u) e^{ila}. \quad (27)$$

We first rearrange Eq. (26):

$$\Psi^*\Psi = \sum_{-\infty<s,n'<\infty} (i)^s J_{n'}(\phi_2) J_{n'-s(N+1)}(\phi_2) e^{-isqv_0\Delta t} e^{i\omega_q s^2 N(NT+\Delta t)} e^{isqx} e^{-i\omega_q st_0(2n'-s)}$$
$$\times \sum_{-\infty<n<\infty} e^{-i\omega_q s^2 N\Delta t} e^{-2i\omega_q sn\Delta t} J_n(\phi_1) J_{n+sN}(\phi_1) (|a|^2 e^{\gamma} + |b|^2 e^{-\gamma}). \quad (28)$$

We now use the identity Eq. (27) with $l=n$, $v=sN$, $u=\phi_1$, $a=-2i\omega_q s\Delta t$ to obtain

$$\Psi^*\Psi = \sum_{-\infty<s,n'<\infty} (i)^s J_{n'}(\phi_2) J_{n'-s(N+1)}(\phi_2) e^{-isqv_0\Delta t} e^{i\omega_q s^2 N(NT+\Delta t)} e^{isqx} e^{-i\omega_q st_0(2n'-s)} (i)^{sN} J_{sN}[2\phi_1 \sin(-\omega_q s\Delta t)] (|a|^2 e^{\gamma} + |b|^2 e^{-\gamma})$$
$$= \sum_{-\infty<n'<\infty} e^{is^2\omega_q t_0(N+1)} J_{n'}(\phi_2) J_{n'-s(N+1)}(\phi_2) e^{-2in'\omega_q st_0} \sum_{-\infty<s<\infty} (i)^{s+sN} e^{-iv_0 sq\Delta t} e^{isqx} J_{sN}[2\phi_1 \sin(-\omega_q s\Delta t)] (|a|^2 e^{\gamma} + |b|^2 e^{-\gamma}). \quad (29)$$

Using Eq. (27) again, this time with $l=n'$, $v=-s(N+1)$, $u=\phi_2$, $a=-2s\omega_q t_0$,

$$\Psi^*\Psi = \sum_{-\infty<s<\infty} e^{-iv_0 sq\Delta t} e^{isqx} J_{-s(N+1)}(2\phi_2 \sin - s\omega_q t_0) J_{sN}[2\phi_1 \sin(-\omega_q s\Delta t)][|a|^2 e^{\gamma} + |b|^2 e^{-\gamma}]. \tag{30}$$

Since the readout pulse is only sensitive to this spatial harmonic, we add only the terms with spatial frequency q:

$$\begin{aligned}\Psi^*\Psi_{detected} = {} & 2(-1)^N J_N[2\phi_1 \sin(-\omega_q \Delta t)] J_{N+1}\{2\phi_2 \sin[(-\omega_q(NT+\Delta t)]\}) \\ & \times \left[|a|^2 \cos\left(q(x - v_0\Delta t) + \frac{eM\hbar q}{4m_{Rb}m_e}[(N^2+N)T^2 + (2N\bar{\tau} + 2N\Delta t + 2\Delta t)T + 2\Delta t(\tau+\bar{\tau}) + \Delta t^2] \right) \right. \\ & \left. + |b|^2 \cos\left(q(x - v_0\Delta t) - \frac{eM\hbar q}{4m_{Rb}m_e}[(N^2+N)T^2 + (2N\bar{\tau} + 2N\Delta t + 2\Delta t)T + 2\Delta t(\tau+\bar{\tau}) + \Delta t^2] \right) \right].\end{aligned} \tag{31}$$

This equation pertains to a single atom with initial velocity v_0 in the x direction. To calculate the signal from our sample, we integrate this result over the Maxwell-Boltzmann velocity distribution. We also substitute $N=1$ to correspond with the time $t \sim 2T$ at which we observe the echo signal in our experiment:

$$\begin{aligned}\langle \Psi^*\Psi_{detected} \rangle_{MB} \propto {} & J_1[2\phi_1 \sin(-\omega_q \Delta t)] J_2\{2\phi_2 \sin[-\omega_q(T+\Delta t)]\} \Big[|a|^2 \cos\Big(qx + \tfrac{eM\hbar q}{4m_{Rb}m_e}[2T^2 + (2\bar{\tau} + 4\Delta t)T + 2\Delta t(\tau+\bar{\tau}) + \Delta t^2] \Big) \\ & + |b|^2 \cos\Big(qx - \tfrac{eM\hbar q}{4m_{Rb}m_e}(2T^2 + (2\bar{\tau} + 4\Delta t)T + 2\Delta t(\tau+\bar{\tau}) + \Delta t^2) \Big) \Big] e^{-q^2u^2\Delta t^2/2}.\end{aligned} \tag{32}$$

Here u is the average atomic speed in the x direction.

Since the signal is backscattered from all atoms in our sample, we must also average this expression over the initial spin states of the atoms. As discussed in Sec. II, we take the initial magnetic sublevel of all atoms to be $m=3$. This implies that the spin state of each atom is spin up with respect to the local magnetic field. With respect to our fixed x axis, the average normalized initial spin state is

$$\begin{pmatrix} \frac{1}{\sqrt{2}} \\ \frac{1}{\sqrt{2}} \end{pmatrix}$$

due to the symmetry. If we take all atoms to be in the $m=-3$ state the same result applies. Substituting $a=b=\frac{1}{\sqrt{2}}$ into the above, we obtain

$$\begin{aligned}\langle \Psi^*\Psi_{detected} \rangle_{MB} & \\ \propto {} & \cos(qx) e^{-q^2u^2\Delta t^2/2} \\ & \times J_1[2\phi_1 \sin(-\omega_q \Delta t)] J_2\{2\phi_2 \sin[-\omega_q(T+\Delta t)]\} \\ & \times \cos\left(\frac{eM\hbar q}{4m_{Rb}m_e}[2T^2 + (2\bar{\tau} + 4\Delta t)T + 2\Delta t(\tau+\bar{\tau}) + \Delta t^2] \right).\end{aligned} \tag{33}$$

The argument of the second-order Bessel function can usually be taken to be $-\omega_q T$ as in Ref. [2], since $\omega_q \Delta t \ll 1$. This expression predicts the signal amplitude to scale as $\cos\left(\frac{eM\hbar q T^2}{2m_{Rb}m_e}\right)$, since Δt, τ, $\bar{\tau}$ can be taken to be small compared to T. Equation (33) also shows a linear dependence of the frequency of oscillations on the magnetic field gradient. Figure 2 shows a plot of the predicted signal amplitude modu-

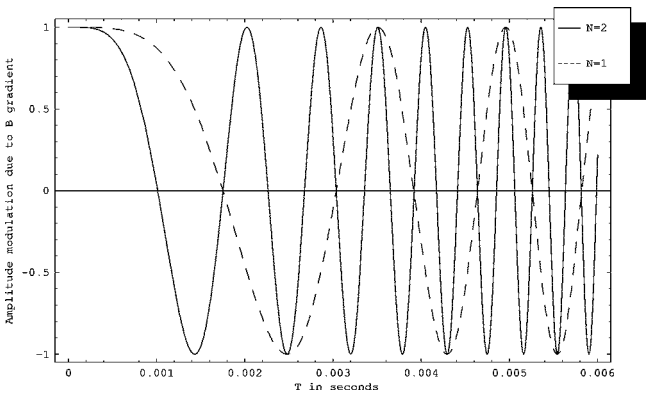

FIG. 2. Predicted oscillatory dependence of echo amplitude for $N=1$ and $N=2$. Here we do not consider the decay of the signal, and we also take $\tau=\bar{\tau}=\Delta t \simeq 0$.

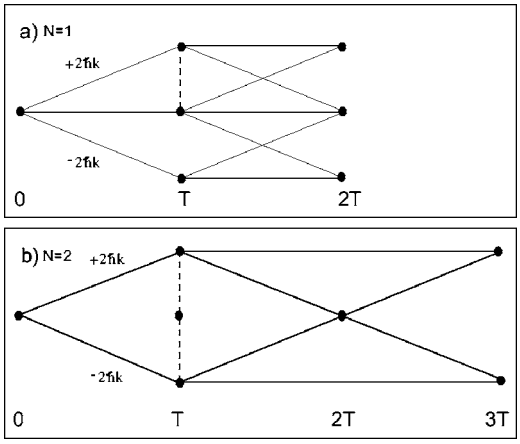

FIG. 3. Recoil diagrams for some of the paths of our interferometer, showing the spatial separation of the interfering wave packets as a function of time.

lation $\cos\left(\frac{eM\hbar q(N^2+N)T^2}{4m_{Rb}m_e}\right)$ for $N=1$ and $N=2$. This expression predicts a different frequency of oscillation for higher-order echoes which occur at $NT+\Delta t$ for $N=2,3\ldots$. If we consider the recoil diagrams associated with our interferometer as in Refs. [26–28], then this predicted dependence on N and T scales as the area between the interfering paths. Figure 3 shows this area dependence for $N=1$ and $N=2$ for some of the possible paths of our interferometer. Note that for any value of N, the area between any interferometer paths that we observe can be divided into two triangles which share a common base (this is shown in Fig. 3 as a dotted line) of length $NvT=\frac{2N\hbar kT}{m}$. Using the heights of these two triangles (T and NT, respectively), we obtain the area A between the paths, $A=\frac{N\hbar kT}{m}(T+NT)\propto(N+N^2)T^2$.

Finally, we note that the calculation suggests that there is no systematic effect due to the magnetic gradient on the atomic recoil frequency. This is consistent with observations in Ref. [7].

A similar calculation shows that the signal also exhibits a dependence on the potential due to gravity $H_g=-mgx$. In the presence of gravity alone, the signal is given by

$$\begin{aligned}\langle\Psi^*\Psi_{detected}\rangle_{MB} &\propto (-1)^N J_N[2\phi_1\sin(-\omega_q\Delta t)]\\ &\times J_{N+1}\{2\phi_2\sin[-\omega_q(NT+\Delta t)]\}e^{-q^2u^2\Delta t^2/2}\\ &\times\cos\Bigg(qx-\frac{qg}{2}[(N^2+N)T^2+(2N\bar{\tau}+2N\Delta t\\ &+2\Delta t)T+2\Delta t(\tau+\bar{\tau})+\Delta t^2]\Bigg).\end{aligned}\tag{34}$$

Here the phase $\frac{gq(N^2+N)T^2}{2}$ is proportional to the area between the paths on a recoil diagram, which is well known [2,26–28]. Both gravity and the magnetic field gradient are predicted to cause T^2 oscillations in the signal.

We can consider the expressions in Eqs. (34) and (33) to be in the form $A(T,\Delta t)\cos\{[q(x-x_0(T,\Delta t)]+\delta(T)\}$, where A is the amplitude, δ is the phase, and $v=\frac{dx_0}{d\Delta t}$ is the velocity. The acceleration of the grating due to gravity causes a time dependent Doppler shift in the backscattered light which can be found using the velocity $v=g(NT+T+\Delta t+\tau+\bar{\tau})$ from Eq. (34).

The difference between the gravity and the magnetic field gradient predictions is that the gravity affects only the phase of the grating and not the amplitude, whereas the magnetic field gradient affects only the amplitude and not the phase (in this case, $\delta=v=0$). As a result, a precise gravity measurement relies on the signal phase but the effect of gravity will also cause a change in the echo signal envelope. In contrast the effect of a magnetic gradient can be inferred from the signal amplitude. The reason for this distinction is that all atoms in the trap experience the same effect from gravity, whereas the effect of the magnetic field gradient depends on the initial spin state of the atoms with respect to the x axis. With all atoms in one m state it is necessary to average over the spin states as in Eq. (33). We note that if all atoms start out in a spin-up state with respect to our x axis [i.e., if we take $a=1$, $b=0$ in Eq. (32)], then both effects are qualitatively identical except that they occur on different time scales. This situation could be realized by turning on a weak quantizing magnetic field and applying laser pulses to optically pump the atoms into one magnetic sublevel.

The expected phase dependence for gravity is $2gkT^2\sim\left(\frac{T}{80\mu s}\right)^2$, whereas the amplitude oscillation for a magnetic field gradient of 0.1 G/cm goes as $\frac{eM\hbar qT^2}{2m_{Rb}m_e}\sim\left(\frac{T}{1ms}\right)^2$. We now briefly outline the experiment and compare our predictions to the data.

III. EXPERIMENTAL DETAILS

Light from a CW Ti:sapphire laser locked to the $F=3\rightarrow F'=4$ transition in ^{85}Rb is routed through a chain of acousto-optic modulators (AOMs) to derive laser frequencies used for cooling and trapping and for atom interferometry. The typical excitation pulse widths are $\sim$500 ns. A grating stabilized diode laser is used to optically pump the atoms into the $F=3$ ground state. The AOMs can be gated on or off using a network of radio frequency (rf) circuits that are controlled by precision delay generators. Rb vapor contained in a vacuum chamber is cooled from room temperature and loaded into a magneto-optical trap [29]. Under typical operating conditions approximately 10^8 atoms are loaded into the trap in $\sim$100 ms. After turning off the anti-Helmholtz coils used for trapping (on a time scale of $\sim$500 μs), the trapping laser beams are further detuned from their normal value of $-\sim2\Gamma$ to a further red detuned value of $\sim6\Gamma$ to cool the atoms in a molasses. Here $\Gamma=5.9$ MHz is the linewidth of the cycling transition. The atoms are held in a molasses for $\sim$5 ms so that the sample is cooled be polarization gradients. The atom interferometer pulse sequence is applied after the turn off of the light used for polarization gradient cooling.

To detect the distribution of atoms in the $F=3$ sublevel, we turned on a bias field of a few and measured the absorption of a probe laser scanned over the $F=3$ to $F=4$ resonance. It was possible to confirm that over 80% of the atoms were present in the $m=\pm3$ states.

The basic experimental arrangement is shown in Fig. 4. Light from a Ti:sapphire laser is directed through an AOM operating at 250 MHz. The undiffracted light from the AOM is used as an optical local oscillator (LO). The LO is aligned through the same optics as the diffracted beam from the AOM and is spatially separated by approximately 2.5 cm from the diffracted beam as shown in Fig. 4. Both beams are incident on a retroreflecting mirror. A shutter is placed in the diffracted beam between the trapped sample and the retroreflecting mirror. The shutter is closed at the time of the readout pulse to avoid standing-wave excitation. An additional AOM is placed in the beam path before the 250-MHz AOM. This AOM is turned on only at the time of the excitation pulses and at the time of the readout pulse in order to minimize the effects of scattered light.

When the readout pulse is applied, the backscattered signal is combined with the LO on a balanced heterodyne detection system to measure the in-phase and quadrature components. The signals are then mixed with the rf used to drive the 250 MHz AOM in order to get the dc components. We

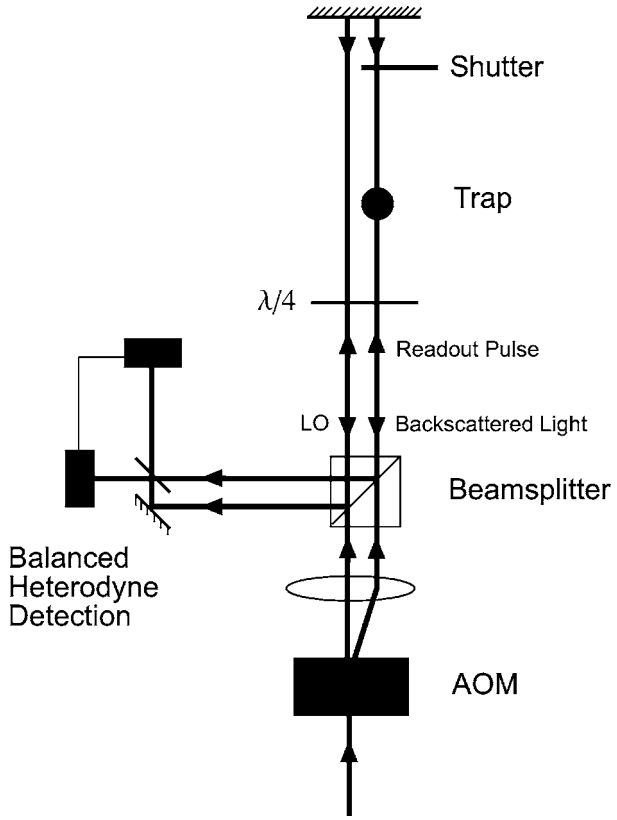

FIG. 4. Experimental setup.

integrate the sum of the squares of the two components over the duration of the signal and take the square root. This quantity scales with the amplitude of the signal and can be studied as a function of T to understand the effects of a magnetic field gradient. To improve signal to noise, we typically average over ten or more repetitions. An alternate method of improving the signal to noise is to use a photomultiplier tube instead of the balanced heterodyne detector to measure the backscattered single intensity. This method does not require the optical local oscillator and can be used in measurements such as the atomic recoil frequency [7] that rely only on the signal amplitude.

To study the effects of gravity, we record the in-phase and quadrature components of the backscattered electric field on a single repetition of the experiment using the optical local oscillator and determine the relative phase. The dependence of the phase on T can be used to extract gravitational acceleration. The echo signal has a dispersion shape with a zero crossing at $2T$ as predicted by Eq. (1). To extract the phase, we determine the signal strength by integrating the first half of the signal and then subtracting the integration of the second half. The phase δ is determined by taking the signal strength associated with each channel as the real and imaginary components of a complex number, x_1 and y_1, such that $x_1+iy_1=e^{i\delta}$. Since the phase of the mirrors is not stabilized during the experiment, it was not possible to average over several repetitions.

The experiment was carried out in a SS316 chamber. The walls of this chamber become magnetized due to the constant pulsing of the anti-Helmholtz coils used to trap the atoms.

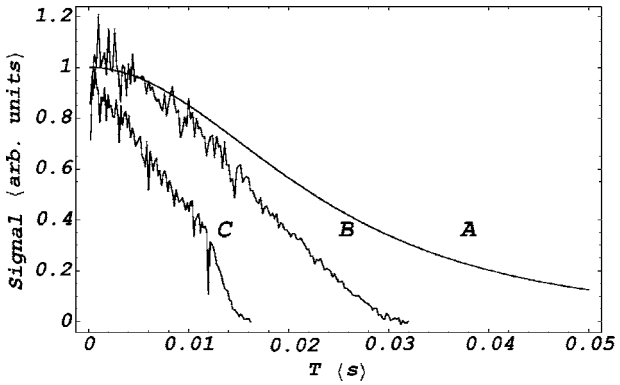

FIG. 5. Decay of the signal amplitude. Curve A is the predicted time of flight signal for 100-μK atoms and 3-mm-diameter excitation beams. Curve B is the signal as a function of time after trap turn off for T fixed at $\sim$28 μs. Curve C is the echo decay measured by fixing the first pulse 2 ms after the trap is turned off, and then moving the second excitation pulse and the readout pulse.

This results in a nonzero field gradient at the location of the trapped cloud even after the current to the anti-Helmholtz coils is turned off. We therefore use an additional set of canceling anti-Helmholtz coils to vary the field gradient present during the experiment.

IV. RESULTS AND DISCUSSION

The data presented here pertain to the $N=1$ ($t\sim 2T$) echo. Figure 5 shows the echo signal decay as a function of T. Curve A is a time-of-flight curve which is modeled using a simulation that depends on measurements of the size of the excitation beams and the temperature of the cloud [30]. Curve B is the decay obtained by setting $T\sim 28$ μs [first maximum of the Bessel function as described in Eq. (1)], and moving the excitation and readout pulses with respect to the time at which the trap is turned off. Curve C is the echo decay showing the effects of decoherence and is measured by fixing the first pulse 2 ms after the trap is turned off, and then moving the second excitation pulse and the readout pulse. The shape of this curve depends on the effect of collisions with background rubidium atoms, scattered light and magnetic field gradients. It can be modeled as a Gaussian in the absence of these effects. Measurements of the recoil frequency were carried out in Ref. [7] under these conditions. The disagreement between curves A and B is attributed primarily to cloud launching effects due to misalignment of the trapping beams.

If a magnetic field gradient is present we observe a characteristic oscillatory decay shown in Fig. 6. These data were recorded in the temperature range 50–70 μK. The fit function is $e^{-t/s_1}[1+s_2\cos(s_3T^2)]s_4$, with oscillations determined by the fit parameter $s_3=0.1671\pm0.0009\times10^6$ s^{-2}. Due to the method by which the data are processed (as described in Sec. III) the signal is strictly positive. Equation (33) predicts the oscillation parameter $s_3'=0.52\times10^6$ s$^{-2}\simeq 6.2s_3$. Although the characteristic effect predicted by the theory is observed in this experiment, we note that the precision in the value of $s3$ is only $\sim$0.5%. We note that the best gradient sensors are

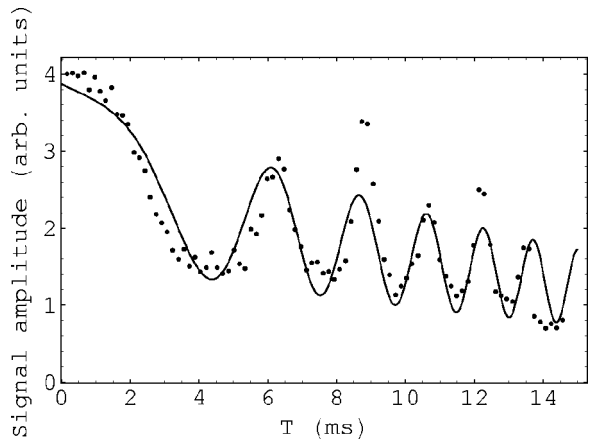

FIG. 6. Oscillatory decay in the absence of a canceling magnetic field gradient. The fit function is $e^{-t/s_1}[1+s_2\cos(s_3T^2)]s_4$, with $s_3 = 0.1671 \pm 0.0009 \times 10^6\ \mathrm{s}^{-2}$. Our theoretical prediction differs from this value by a factor of ~6.2. The smooth decay in curve *C* of Fig. 5 is obtained by canceling this gradient.

sensitive to gradients that are several orders of magnitude smaller [31]. The fit function used in Fig. 6 also includes an exponential which models the time-of-flight decay, an effect that is not included in the theoretical treatment leading to Eq. (33).

Figure 7 shows a plot of the oscillation parameter s_3 as a function of the magnetic field gradient. The linear dependence predicted by Eq. (33) is observed. The minimum value on this curve represents the external gradient which cancels the gradient due to the magnetization of the chamber. It is for this canceling gradient that we observe a smooth decay such as the one shown in curve *C* of Fig. 5. In Fig. 7 we have fit to the function $|aM+b|$ by taking the data point at the lowest value of the *B* field gradient and reflecting it about the horizontal axis so that a linear regression may be used. The fit gives $a = 3.42 \pm 0.06 \times 10^6\ \mathrm{s}^{-2}\ \frac{\mathrm{G}}{\mathrm{cm}}$ and $b = 0.168 \pm 0.002 \times 10^6\ \mathrm{s}^{-2}$. When no canceling gradient is applied, we observe a nonzero oscillation parameter s_3 as shown in Figs. 6 and 7. Equation (33) predicts the value $a' = 1.06 \times 10^7\ \mathrm{s}^{-2}\ \frac{\mathrm{G}}{\mathrm{cm}} \simeq 6.2a$.

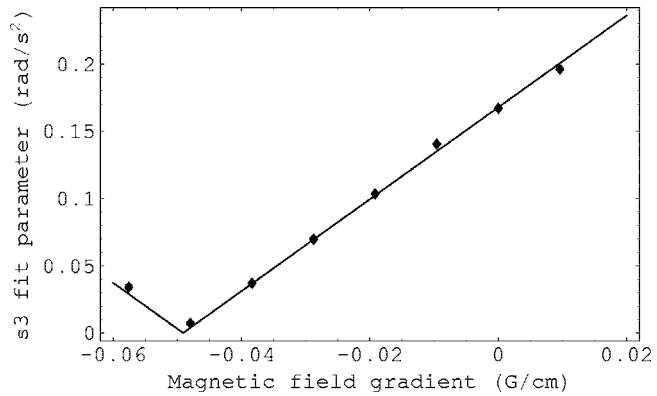

FIG. 7. Linear dependence on canceling magnetic field gradient. The fit function is $|aM+b|$, where $a = 3.42 \pm 0.06 \times 10^6\ \mathrm{s}^{-2}\ \frac{\mathrm{cm}}{\mathrm{G}}$ and $b = 0.168 \pm 0.002 \times 10^6\ \mathrm{s}^{-2}$. The theoretical value for the slope differs by a factor of ~6.2.

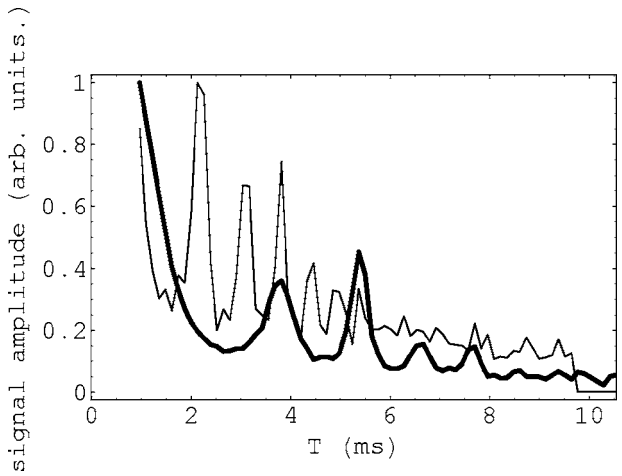

FIG. 8. Oscillatory decay for the echoes at $t=2T$ (thick line) and $t=3T$ (thin line) for the same magnetic field gradient. These are labeled $N=1$ and $N=2$ in Fig. 2, respectively. The fit function used in Fig. 6 gives $s3 = 0.434 \pm 0.005 \times 10^6\ \mathrm{s}^{-2}$ for $N=1$ and $1.293 \pm 0.004 \times 10^6\ \mathrm{s}^{-2}$ for $N=2$. Thus the oscillation frequency for the $N=2$ echo is three times the oscillation frequency for the $N=1$ echo which is consistent with predictions in Sec. II. The amplitudes of the two echo decays have been normalized to the maximum amplitude of each decay curve. The $N=2$ echo amplitude is typically a factor of 4 smaller than the amplitude of the $N=1$ echo.

The theoretical values for s_3' and a' are determined by assuming the field due to the magnetized chamber to be identical to the quadrupole field applied by the canceling coils. In particular, $s_3' = \frac{eM\hbar qT^2}{2m_{Rb}m_e}$ is determined by using the value of the magnetic field gradient due to the canceling coils at the minimum value of the linear fit in Fig. 7. Although the theory predicts the qualitative linear dependence on *M* and oscillatory T^2 dependence, there is quantitative disagreement. We also do not have a satisfactory explanation for the alternating height of the peaks in Fig. 6. A possible explanation for the offset in this figure could be incomplete optical pumping in the $|m|=3$ sublevels.

We note that a simple physical model can also be used to predict the oscillatory signal amplitude due to the gradient. In the presence of a magnetic gradient the phase accumulation for the recoil components in Fig. 3 depends on the spatial separation and the magnetic field gradient. The phase difference between recoil components at the echo points can be shown to scale as MT^2. This treatment also gives the same oscillation parameter predicted by the theoretical model which results in Eq. (33).

Figure 8 shows the period of oscillations induced by a magnetic gradient for the $N=1(t=2T)$ and $N=2(t=3T)$ echoes discussed in Sec. II. Theoretical fits described in the figure caption confirm that the frequency of oscillations scales as $N(N+1)$ as predicted by Eq. (33) and described in Fig. 2.

We have also investigated the oscillatory dependence of the $N=1$ echo for a fixed magnetic gradient over the range of cloud temperatures accessible in the experiment (between ~15 and 150 μK). The results show that the oscillation frequency is independent of the temperature.

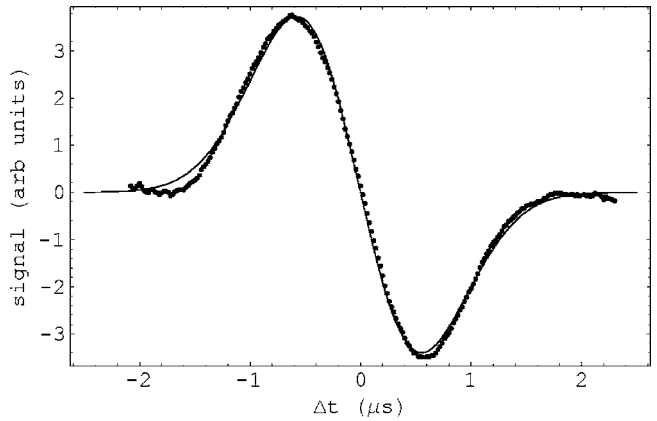

FIG. 9. The signal at a fixed value of T, with a fit to $a_1 \Delta t e^{-(\Delta t/a_2)^2}$ based on 1.

We attribute the quantitative disagreement between theory and experimental data to the simplifications in our model. In particular, we expect that effects due to the three-dimensional nature of the actual experiment play a role. The calculation does not consider situations in which the atoms do not cross the center of the trap, in which case it is possible for the dipole moment to adiabatically follow the B field. Under typical experimental conditions we expect a majority of the atoms to avoid the center of the trap. Even at the lower range of our cloud temperature, the fraction of atoms that pass through the center is fairly small. This could explain the independence of the oscillation frequency on the cloud temperature. In addition, the comparison between experiment and theory relies on the assumption that the field due to the magnetization of the chamber is a quadrupole field. There is also a small possibility that the disagreement could also be due to this assumption since this field cannot be measured directly.

Figure 9 shows the dispersion signal shape at a fixed value of $T \sim 1$ ms predicted by Eq. (1). If the time between when the trap is turned off and the readout pulse is increased, we observe a change in shape of the echo envelope which arises because of the motion of the cloud under the influence of gravity, as given by Eq. (34). The detection technique allows the Doppler shift to be observed as a change in the shape of the echo envelope. Detailed quantitative comparisons are not possible because the signal phase varies on every repetition due to mirror vibrations. Equation (34) predicts the Doppler shift of the backscattered light due to gravity to be dependent on T and Δt. In addition, we expect that the shift depends on the time between trap turnoff and the first standing-wave pulse, and the initial velocity due to cloud launch. These factors are not explicitly included in the theory leading to Eq. (34). The Doppler shift is expected to lead to extra zero crossings in the final signal (for fixed T). Figure 10 shows a fit to the dispersion signal using a functional form based on the Doppler shift. The fit function used in Fig. 10 differs from that used in Fig. 9 by a cosine term whose frequency represents the expected Doppler shift. The fit parameter $a5$ represents the point $\Delta t = 0$. We find the fits to be qualitatively consistent with our data, as shown in Fig. 10. If the stability of the inertial frame of reference is improved,

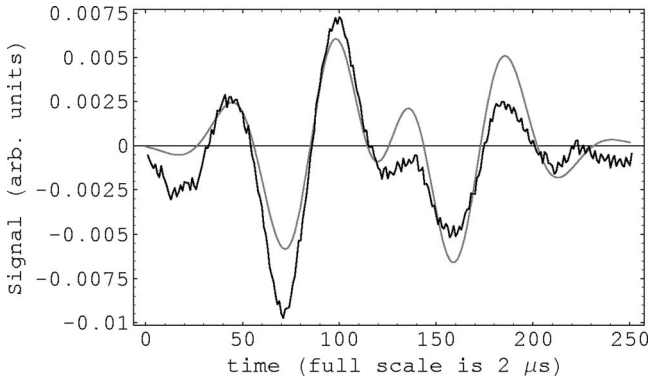

FIG. 10. One component of the signal envelope for a fixed value of T, showing the effect of the Doppler shift due to gravity. The fit function $a_1(t-a_5)\cos[a_4+(\frac{1+(g/c)(a_3+t-a_5)}{1-(g/c)(a_3+t-a_5)}-1)\omega(t-a_5)]e^{-[(t-a_5)]/a_2]^2}$ is based on Eq. (34).

we expect to obtain better quantitative agreement with the data and improve precision in gravity measurements. It is interesting to note that if mirror vibrations and launch effects can be controlled, it may be possible to extract the value $\frac{g}{c}$ from the Doppler shift.

Figure 11 shows the relative phase of the signal as a function of the pulse separation T as well as the corresponding parabolic fit to qgT^2 as in Eq. (34). The average spacing between points is ~ 3 μs. Since the standard deviation of the residuals is $\sim \pm 1$ rad, this leads to a precision of ~ 15 ppm. Although the residuals from our data are larger than those in Ref. [2] due to the effect of mirror vibrations over the time scale of the experiment, we obtain higher precision due to the much longer time scale of our experiment. We note that the gravity measurements were carried out with the excitation beams aligned to within 1 mrad of 180°. However, the orientation with respect to the vertical could not be independently verified. The measured value of g was found to be affected by the presence of residual magnetic field gradients. This systematic effect has not been fully explored. Nevertheless, the extent of the variation rules out alignment effects as the cause.

It is clear that the precision can be substantially improved by determining the functional form of the echo envelope and extracting a better phase measurement from a fit. This could

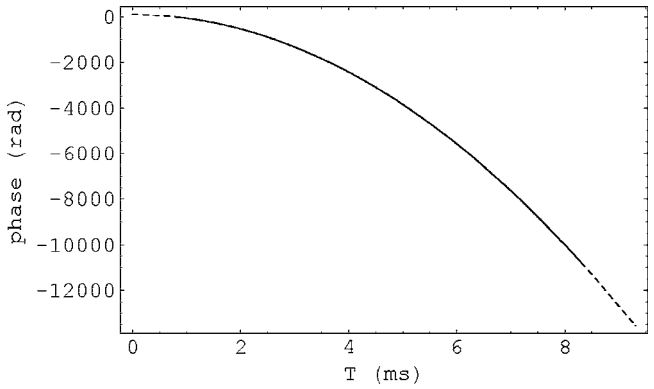

FIG. 11. Relative phase of signal as a function of T. A parabolic fit (dashed line) gives the value $g = 9.792\,05 \pm 0.000\,15$ m/s^2.

result in a measurement of g that is precise at the level of $\sim$100 ppb which would make it feasible to measure the effect of tidal forces. Fitting to the signal envelope is also crucial for fountain based measurements precise to $\sim$1 ppb. These improvements can only be achieved by stabilizing the retroreflecting mirror that serves as the inertial frame of reference as in Ref. [9]. This constitutes the most important technical challenge for future work.

V. CONCLUSIONS

We have presented a complete discussion of a simplified theoretical model which predicts the effects of a magnetic field gradient and gravity on an echo-type single state atom interferometer. The results are expected to be of interest to all single state interferometers that are being developed for precision measurements of atomic recoil and gravity. Experimental results confirm the scaling laws predicted by the theory although the discrepancy between theory and experiment for the oscillation frequency of the signal amplitude is not understood. The discrepancy could potentially arise because the calculation does not take into account the three-dimensional nature of the experiment or the effects of spontaneous emission on the signal shape. A more comprehensive theoretical model could include these effects. The experiment could also be carried out at lower temperatures to decrease the fraction of atoms which adiabatically follow the magnetic field.

It is also been possible to verify the predictions for the oscillatory dependence of the amplitudes of higher-order echoes. The calculations clearly show that there are no systematic changes to the recoil frequency due to the gradient which is consistent with Ref. [7]. However, the experiment has to be isolated from magnetic gradients so that the signal amplitude can be recorded over a long time scale. For a fountain experiment with a time scale of $\sim$200 ms the magnetic gradients should be reduced to the level of $\sim 2\times 10^{-5}\ \frac{\mathrm{G}}{\mathrm{cm}}$. Since the source of the gradient in this experiment is the magnetized vacuum chamber, it should be possible to shield gradients to the desired level by using a nonmagnetic chamber and conventional techniques using mu metal shields. This would make it feasible to study systematic effects such as index of refraction and wave-front curvature and complete a measurement of the recoil frequency precise to a few parts per billion. An alternate method of reducing magnetic effects is to use atoms in the $m=0$ state, as in experiments using Raman interferometers.

In recent studies the vacuum chamber used in this experiment (SS 304) has been replaced with a nonmagnetic chamber (SS 316). We have observed long lived decays on a time scale of $\sim$30 ms which is a significant improvement in comparison with curve *C* of Fig. 5. It is notable that the canceling magnetic gradients necessary to obtain such decays are $\sim$10 times smaller than the canceling gradient used previously. The dominant contribution to the residual gradient is presently associated with stray magnetic fields from a nearby ion pump. This suggests that higher-order contributions to the magnetic field (which are not considered in our theoretical treatment) are unlikely to affect the experiment. To incorporate such higher-order terms in a theoretical framework, it will be necessary to adopt a different method of carrying out this calculation or to use numerical techniques.

We have also presented an improved measurement of gravitational acceleration using echo techniques. The calculation correctly predicts the well-known T^2 scaling law for phase accumulation due to gravity. This result is in agreement with a previous calculation based on the principle of least action [4]. Since the mathematical form of the calculations due to the gradient and gravity are very similar, the agreement suggests that three-dimensional effects play a significant role in experiments with magnetic field gradients.

Our results show that understanding the shape of the echo envelope is crucial for improving the precision of phase measurements to determine gravitational acceleration. We expect to obtain improved fits to the signal shape by stabilizing the mirror that serves as the inertial frame of reference. This would constitute the most significant technical challenge in future work following which atoms could be launched in an atomic fountain. This would make it feasible to consider measurements precise at the level of $\sim$1 ppb.

ACKNOWLEDGMENTS

This work was supported by CFI, OIT, PRO, NSERC, and York University.

[1] D. S. Weiss, B. C. Young, and S. Chu, Phys. Rev. Lett. **70**, 2706 (1993).
[2] S. B. Cahn, A. Kumarakrishnan, U. Shim, T. Sleator, P. R. Berman, and B. Dubetsky, Phys. Rev. Lett. **79**, 784 (1997).
[3] S. Gupta, K. Dieckmann, Z. Hadzibabic, and D. E. Pritchard, Phys. Rev. Lett. **89**, 140401 (2002).
[4] A. Wicht *et al.*, *Proceedings of the 6th International Symposium on Frequency Standards*, edited by P. Gil (World Scientific, Singapore, 2002), p. 193.
[5] M. Weel and A. Kumarakrishnan, Phys. Rev. A **67**, 061602(R) (2003).
[6] R. Battesti, P. Clade, S. Guellati-Khelifa, C. Schwob, B. Gremaud, F. Nez, L. Julien, and F. Biraben, Phys. Rev. Lett. **92**, 253001 (2004).
[7] M. Weel, S. Beattie, I. Chan, E. Rotberg, A. Vorozcovs, and A. Kumarakrishnan (unpublished).
[8] M. Kasevich and S. Chu, Phys. Rev. Lett. **67**, 181 (1991).
[9] A. Peters, K. Y. Chung, and S. Chu, Nature (London) **400**, 849 (1999).
[10] T. L. Gustavson, P. Bouyer, and M. A. Kasevich, Phys. Rev. Lett. **78**, 2046 (1997).
[11] J. M. McGuirk, G. T. Foster, J. B. Fixler, M. J. Snadden, and M. A. Kasevich, Phys. Rev. A **65**, 033608 (2002).
[12] B. Taylor, Metrologia **31**, 181 (1994).

[13] R. S. Van Dyck, P. B. Schwinberg, and H. G. Dehmelt, Phys. Rev. Lett. **59**, 26 (1987).
[14] G. K. Campbell, A. E. Leanhardt, J. Mun, M. Boyd, E. W. Streed, W. Ketterle, and D. E. Pritchard, Phys. Rev. Lett. **94**, 170403 (2005).
[15] J. Ye, S. Swartz, P. Jungner, and J. L. Hall, Opt. Lett. **21**, 1280 (1996).
[16] M. P. Bradley, J. V. Porto, S. Rainville, J. K. Thompson, and D. E. Pritchard, Phys. Rev. Lett. **83**, 4510 (1999).
[17] Y. J. Wang, D. Z. Anderson, V. M. Bright, E. A. Cornell, Q. Diot, T. Kishimoto, M. Prentiss, R. A. Saravanan, S. R. Segal, and S. Wu, Phys. Rev. Lett. **94**, 090405 (2005).
[18] S. Fray, C. A. Diez, T. W. Hansch, and M. Weitz, Phys. Rev. Lett. **93**, 240404 (2004).
[19] M. J. Snadden, J. M. McGuirk, P. Bouyer, K. G. Haritos, and M. A. Kasevich, Phys. Rev. Lett. **81**, 971 (1998).
[20] M. Weel, S. Beattie, I. Chan, E. Rotberg, and A. Kumarakrishnan, Bull. Am. Phys. Soc. **50**, 41 (2005).
[21] C. G. Townsend, N. H. Edwards, C. J. Cooper, K. P. Zetie, C. J. Foot, A. M. Steane, P. Szriftgiser, H. Perrin, and J. Dalibard, Phys. Rev. A **52**, 1423 (1995).
[22] A. Vorozcovs, M. Weel, S. Beattie, S. Cauchi, and A. Kumarakrishnan, J. Opt. Soc. Am. B **22**, 943 (2005).
[23] D. V. Strekalov, Andrey Turlapov, A. Kumarakrishnan, and Tycho Sleator, Phys. Rev. A **66**, 023601 (2002).
[24] G. B. Arfken and H. J. Weber, *Mathematical Methods for Physicists* (Harcourt/Academic Press, San Diego, 2001).
[25] M. Suzuki, Commun. Math. Phys. **57**, 193 (1977).
[26] R. Friedberg and S. R. Hartmann, Phys. Rev. A **48**, 1446 (1993).
[27] R. Beach, S. R. Hartmann, and R. Friedberg, Phys. Rev. A **25**, 2658 (1982).
[28] R. Beach, B. Brody, and S. R. Hartmann, Phys. Rev. A **27**, 2537 (1983).
[29] C. Monroe, W. Swann, H. Robinson, and C. Wieman, Phys. Rev. Lett. **65**, 1571 (1990).
[30] I. Yavin, M. Weel, A. Andreyuk, and A. Kumarakrishnan, Am. J. Phys. **70**, 149 (2002).
[31] R. Fitzgerald, Phys. Today **56** (7), 21 (2003), and references therein.